Available online at www.sciencedirect.com
ScienceDirect
Journal of Sound and Vibration 315 (2008) 157–175
JOURNAL OF SOUND AND VIBRATION
www.elsevier.com/locate/jsvi

Investigations of propagating wave types in railway tracks at high frequencies

J. Ryue[a,*], D.J. Thompson[a], P.R. White[a], D.R. Thompson[b]

[a]*Institute of Sound and Vibration Research, University of Southampton, Highfield, Southampton SO17 1BJ, UK*
[b]*Balfour Beatty Rail Technologies, Midland House, Nelson Street, Derby, DE1 2SA, UK*

Received 4 July 2007; received in revised form 6 December 2007; accepted 23 January 2008
Handling Editor: C. Morfey
Available online 3 March 2008

Abstract

At low frequencies waves propagate in a rail as bending, extensional or torsional waves. At higher frequencies, above about 1.5 kHz, the rail cross-section deforms and many higher order wave types exist. This cross-section deformation has to be taken into account for an accurate evaluation of the dispersion properties at high frequencies. Simulation results in the literature show that a multiplicity of wave modes is possible within this high-frequency range. In this work, wave types that propagate primarily through separate regions of the rail cross-section are investigated for frequencies up to 80 kHz. Two numerical methods are applied to obtain the dispersion properties for a railway track model including rail pads as a continuous foundation. These are a conventional finite element (FE) method and a wavenumber finite element (WFE) method, each of which can include the effects of cross-sectional deformation. In order to validate the predicted results, experiments were performed on a short test track using an impact hammer and accelerometers. Additional measurements used piezoceramic transducers to excite the rail at higher frequencies. The results are compared with simulations in terms of the group velocity and they present very good agreement. From this comparison, it is identified which wave types predominantly propagate on various regions of the rail cross-section.
© 2008 Elsevier Ltd. All rights reserved.

1. Introduction

At low frequencies a railway track can be modelled as a simple beam on an elastic support, but at high frequencies above about 1.5 kHz, deformation of the cross-section occurs and multiple wave types are sustained [1]. For noise modelling, investigations have usually been limited to the behaviour below 5 kHz [1–5]. In this frequency range, deformation shapes of propagating waves have been well identified because only a small number of waves are generated there. However, for the purpose of long range rail inspection, it was suggested in literature [6,7] that higher frequencies up to 80 kHz need to be considered. It was also identified that several tens of different wave types are created in this higher frequency range making the dispersion curves very complicated. Because of that, there has been little work aimed at identifying effective wave types

*Corresponding author. Tel.: +44 2380 594930; fax: +44 2380 593190.
E-mail address: jr1@isvr.soton.ac.uk (J. Ryue).

0022-460X/$ - see front matter © 2008 Elsevier Ltd. All rights reserved.
doi:10.1016/j.jsv.2008.01.054

for long range propagation along railway tracks and how to measure them efficiently from multiple wave types in experiments.

Thompson [8] developed an experimental analysis technique for low frequencies below 5 kHz, based on the Prony method [9], which can estimate dispersion curves of propagating waves by using measured data taken on the track. However, this method is not suitable for the frequencies of interest in this study because the number of measuring points required becomes impractical. Hayashi et al. [10] predicted the dispersion relations of a rail up to 100 kHz using a two-dimensional finite element method and compared these results with the measured phase velocity curves obtained by a two-dimensional Fourier transform technique. On the basis of the measured data, they highlighted waves that have large deformations at the top of a rail head among multiple propagating waves. To achieve this they acquired experimental data measured at 200 points along the rail, but the deformation shapes of the highlighted waves were not specified. Wilcox et al. [11] developed equipment using a transducer array along the length of the rail, as well as around the perimeter of the rail cross-section, to excite and detect any wave mode effectively. However, they failed to describe each wave's behaviour with respect to frequency and also did not present what type of waves are most efficient for their purpose.

This study aims to investigate the propagation of waves in a railway track up to 80 kHz. The work presented in this paper concentrates on identifying which wave types propagate effectively along the rail in which part of the rail cross-section. It is not the intention of the paper to provide detailed descriptions of all the waves present below 80 kHz. The purpose of the dispersion curves and group velocities is to show the range of values obtained with all waves, and to show the dominant values measurable at various locations on the rail. As a first step in this study, a finite element model is set up for a rail supported on a rail pad, represented as a continuous elastic foundation. To simulate the waves in an infinite rail, a short length of the rail is modelled with symmetric and/or antisymmetric boundary conditions at both ends of its length. Modal analysis for this short length track will produce natural frequencies and their mode shapes of the rail section. These results are used to obtain the frequency–wavenumber relations, group velocities and the deformation profiles of each wave. Although conventional FE methods can readily be used even at high frequencies, they have several drawbacks for dealing with wave propagation in an infinite length structure. So an alternative numerical method, called the wavenumber finite element (WFE) method, is employed. (This method is also referred to as the waveguide FE method [12,13] or semi-analytical FE method [10,14].) It only requires cross-sectional modelling of a railway track and is computationally much less demanding than conventional FE methods. From these two numerical methods, group velocities of propagating waves are predicted and compared. Then a single quantity is introduced to determine the measurable waves at different positions on the rail surface using the simulated results.

Finally, in order to validate the simulated results, two experiments are conducted on a test track, approximate length 32 m, using different input excitation schemes: an impact hammer and piezoceramic transducers (PZT). Time–frequency analysis is applied to the measured data in order to visualize dispersion relations of the measured waves. The results are compared with the simulated ones in terms of the group velocity and the various wave types are identified.

2. Finite element analysis of a railway track

2.1. Track modelling

In this section, a short length of UIC60 rail is modelled using the finite element package, ANSYS. Since the UIC60 rail has a symmetric cross-section, only half of the width is included as shown in Fig. 1. This has an additional advantage of separating the possible waves into two groups that are uncoupled from each other. That is, a symmetric boundary condition that constrains the deformation of the mid-plane in the y direction gives the vertical and symmetric longitudinal modes; an antisymmetric boundary condition that x and z directions are constrained in the mid-plane gives the lateral and torsional modes as well as the antisymmetric longitudinal modes in which opposite sides of the rail move in opposite directions. The chosen length of the rail model is 0.3 m, which is selected as a half of the usual sleeper span in railway track. The rail clip is generally much more flexible than the rail pad and is omitted from the model [15]. In addition, since the

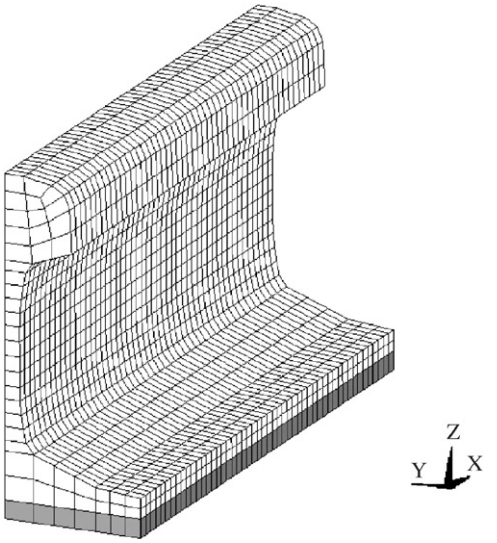

Fig. 1. FE model of a rail on a distributed elastic foundation.

contribution of the sleeper and ballast are limited to the low-frequency region below 1 kHz [15], only the rail pad is included in this model.

In practice, rail pads are placed discretely between the rail and the sleepers. This discrete support induces a strong periodicity effect, so-called ''pinned–pinned resonances'', at low frequencies where wavelengths are longer than the rail pad length and spacing. However, the effect of periodicity resulting from the discrete foundation reduces as frequency increases [2,3]. The discrete foundation can be approximated in the FE modelling by simply compensating the stiffnesses of the foundation for the shorter length of it. Using such discrete rail pads, however, it was found that they make uneven deformation shapes along a rail. Furthermore, they allow different wavelengths in different regions of the rail at some frequencies. This implies that several different wavelengths can coexist at a single frequency. It would, therefore, be difficult to determine frequency–wavenumber relations because wavelengths are not clearly defined in the deformed rail shape. To make matters simpler, the rail pads are modelled as a continuous foundation in this study. Nevertheless, the continuous foundation model seems to be a good approximation of the real situation at high frequencies. That is because the stiffness of the rail pad is much less than that of the rail so that reflections of waves at the start and end of each discrete pad will be insignificant. Also it was confirmed by means of numerical analysis that decay rates of each wave obtained from the continuous and discrete foundation models are very similar at frequencies above 20 kHz.

Fig. 1 shows the FE model created for the track used in this study, which has 50 elements in the length. The stiffnesses of the single rail pad were chosen to be 150 MN/m in the vertical direction and 20 MN/m in the lateral and longitudinal directions. These values are typical of a modern resilient pad [3,8]. At high frequencies, however, the stiffness of the rail pad usually becomes much higher than the static or low-frequency stiffness. This is because the rail pad has mass which leads to internal resonances at high frequencies. Moreover the rubber material itself becomes stiffer at higher frequencies. This stiffness of the rail pad, called the ''dynamic stiffness'' here, is one of the important parameters for track modelling. It could be possible to measure this in the laboratory or directly to model the rail pad with fine finite element layers to capture the dynamic stiffness. Direct FE modelling of the rail pad requires several tens of finite elements in the vertical direction of the pad thickness to be able to express the internal resonance effects. To avoid this complexity, the dynamic stiffness was predicted theoretically from a one-dimensional foundation model. Note that the rail pad may not be uniform, for example studs or ribs are often present on its surfaces. However in the following a uniform structure is considered for simplicity.

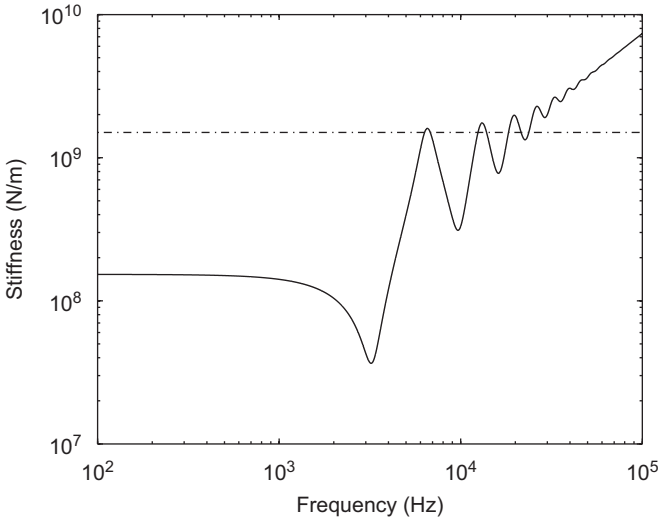

Fig. 2. The stiffness of the rail pad as a function of frequency when $\rho_p = 1000\,\mathrm{kg/m^3}$ and $\eta_p = 0.2$ in Eq. (1). ——, dynamic stiffness calculated; – –, constant stiffness for FE analysis.

The dynamic stiffness of the one-dimensional foundation with thickness h can be expressed as

$$k_{p,z} = \frac{E_{p,z} A \kappa \cos \kappa h}{\sin \kappa h}, \tag{1}$$

where $E_{p,z}$ is the complex elastic modulus of the foundation in the z direction, κ is the complex wavenumber in the z direction, A is the contact area between the rail and foundation [16]. The stiffness, $k_{p,z}$, of the foundation in the vertical direction is illustrated in Fig. 2 as a function of frequency when the density, thickness and damping loss factor of the rail pad are given as $\rho_p = 1000\,\mathrm{kg/m^3}$, $h = 10\,\mathrm{mm}$ and $\eta_p = 0.2$, respectively. As shown in Fig. 2, the stiffness increases with frequency due to the presence of standing waves in the foundation. In the FE analysis it is not feasible to introduce a frequency-dependent stiffness to the modal analysis. Therefore, based on this simulated stiffness, the rail pad is modelled as a massless foundation having constant dynamic stiffnesses which are 10 times larger than the stiffnesses for low frequencies. This will tend to over-emphasise the influence of the pad below 20 kHz and under-emphasise it above this frequency.

2.2. Predicted dispersion relations

To simulate the waves in an infinite rail, the model is solved with symmetric and/or antisymmetric boundary conditions at both ends of the 0.3 m length [1]. The symmetric boundary condition allows two translational motions in the y and z directions, and one rotational motion about the x direction. Conversely the antisymmetric one allows two rotational motions about the y and z directions, and one translational motion in the x direction.

Modal analysis will produce natural frequencies and their mode shapes of the 0.3 m rail section. Each natural frequency and mode shape produced by the modal analysis has a sinusoidal mode shape in the x direction and can be interpreted as the sum of two identical waves which travel in opposite directions and thus form a standing wave in an infinite rail. Each natural frequency and wavelength of these boundary conditions thus corresponds to a point on the frequency–wavenumber relation for an infinite rail. For the symmetric–symmetric (or antisymmetric–antisymmetric) boundary conditions, the wavenumbers in the x direction will be $\kappa = n\pi/L$ and for the symmetric–antisymmetric (or antisymmetric–symmetric) case $\kappa = (2n+1)\pi/2L$ where L is the length of the rail section and n is $0, 1, 2, \ldots$. Therefore, $\Delta\kappa$ in the predicted dispersion relation becomes $\pi/2L$. For a length $L = 0.3\,\mathrm{m}$, this increment is 5.02 rad/m.

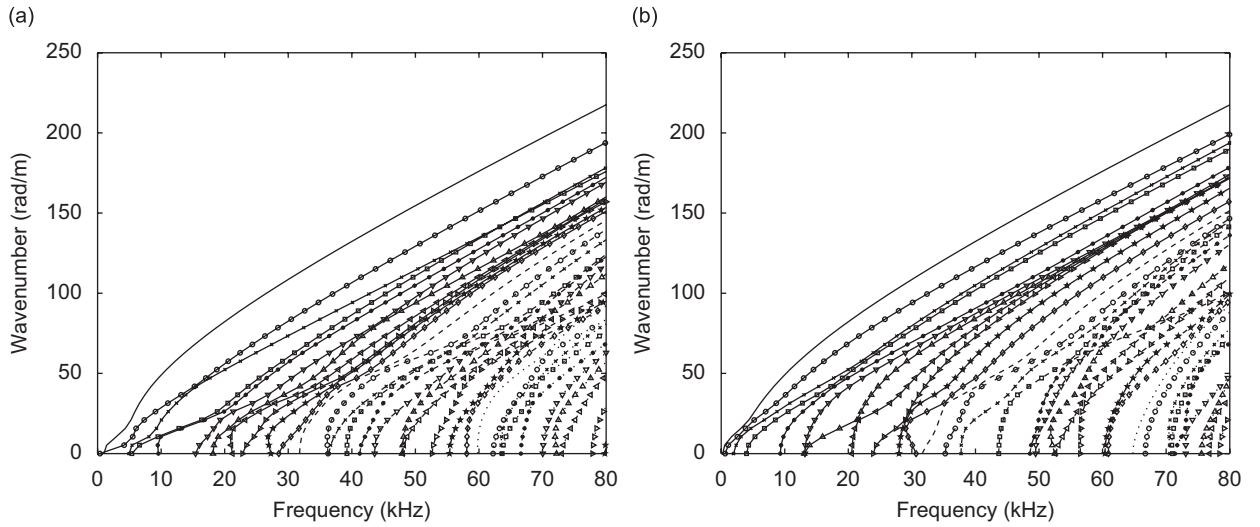

Fig. 3. Predicted dispersion curves for (a) the vertical and symmetric longitudinal waves and (b) the lateral, torsional and antisymmetric longitudinal waves. Each wave is distinguished with various line styles and markers.

Fig. 3(a) illustrates the dispersion curves generated by connecting the discrete frequency–wavenumber points produced from the modal analysis for the vertical and symmetric longitudinal waves. In this figure, the different waves are distinguished with various line styles and markers. Fig. 3(b) shows the corresponding results for the lateral, torsional and antisymmetric longitudinal waves. These figures reveal that there are 63 wave types in total in the rail in the frequency range up to 80 kHz. In this work, each wave type in each figure is referred to by the order of the wavenumber from top to bottom such as the first wave, second wave, etc. in the vertical and symmetric longitudinal waves.

Since the dispersion curves within one of the graphs in Fig. 3 (i.e., symmetric or antisymmetric waves with respect to the mid-plane) do not cross each other, these waves exhibit mode coupling and finally swap their mode shapes when they come close [17]. For example, the second and third waves in Fig. 3(a) approach each other and swap their mode shapes at roughly 5 and 15 kHz. In addition, Fig. 3(a) shows a non-dispersive wave increasing to about 100 rad/m by 80 kHz in the frequency–wavenumber plot, formed by consecutive pieces of different waves with a constant slope. These are non-dispersive longitudinal waves in which the head, web and foot move longitudinally in the same or opposing directions to each other. The phase speed is around 5000 m/s, the longitudinal wave speed in a rod of steel. Furthermore, it seems in Fig. 3(b) that longitudinal wave motions also take place as a group of waves appear with a phase speed around 5000 m/s. These longitudinal waves will have an antisymmetrically deformed mode shapes in the rail with respect to the mid-plane.

Figs. 4 and 5 show the deformation shapes of several waves at around 50 kHz in Fig. 3(a) and (b), respectively. In each case they correspond to the six waves with the highest wavenumbers in Fig. 3. For the vertical and symmetric longitudinal waves, the first, second and fourth waves correspond to the first-, second- and third-order foot bending waves (Fig. 4(a), (b) and (d)). It can be shown from Fig. 3(a) that these convert from the global bending wave at about 5 and 15 kHz, and from the longitudinal wave at about 18 kHz, respectively. In other words, the first wave has global bending deformation below 5 kHz. Whereas, the second wave has the longitudinal deformation below 5 kHz and global bending deformation between 5 and 15 kHz. The third wave is the vertical bending wave in the rail head (Fig. 4(c)) and the fifth and sixth waves appear to be predominantly longitudinal type waves in the foot and rail head, respectively (Fig. 4(e) and (f)). For the lateral and torsional waves, the first and third waves selected are foot bending waves (Fig. 5(a) and (c)) and the second and fourth are the first- and second-order web bending waves (Fig. 5(b) and (d)). The fifth and sixth waves show mixed motions of the rail head and web (Fig. 5(e) and (f)). These examples of deformation shapes

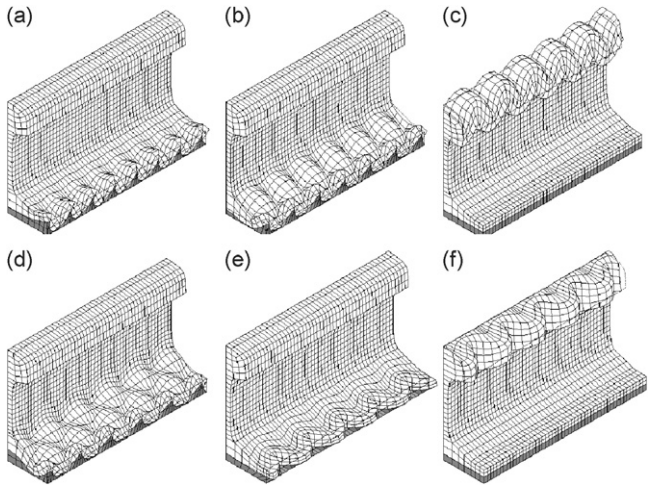

Fig. 4. Deformation shapes of first 6 waves close to 50 kHz for the vertical and longitudinal waves. (a) The first wave at 48,740 Hz, (b) the second wave at 50,719 Hz, (c) the third wave at 50,398 Hz, (d) the fourth wave at 49,626 Hz, (e) the fifth wave at 49,870 Hz and (f) the sixth wave at 50,723 Hz.

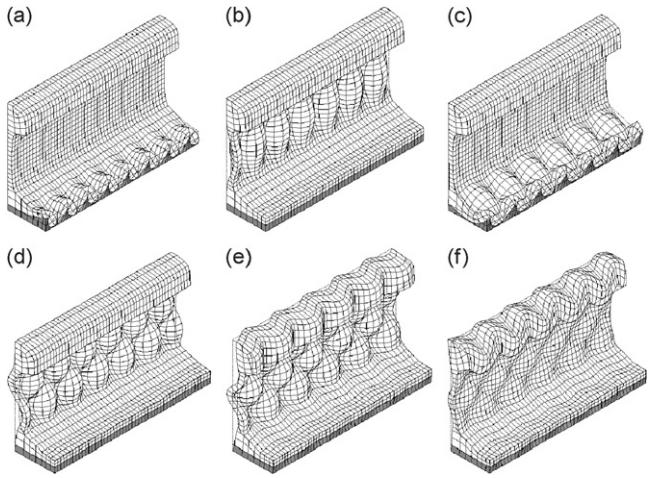

Fig. 5. Deformation shapes of first 6 waves close to 50 kHz for the lateral and torsional waves. (a) The first wave at 51,139 Hz, (b) the second wave at 49,193 Hz, (c) the third wave at 48,793 Hz, (d) the fourth wave at 50,192 Hz, (e) the fifth wave at 49,020 Hz and (f) the sixth wave at 50,505 Hz.

indicate that waves with larger wavenumbers are more likely to propagate through a local region of the rail cross-section. The other wave modes around 50 kHz, having lower wavenumbers, generally have globally coupled deformation shapes in which head, web and foot all vibrate.

The dispersion curves predicted from the supported rail model are compared with those for a free rail in Fig. 6 for frequencies below 20 kHz. This figure shows that the effect of the elastic foundation appears mainly at low frequencies below 10 kHz, resulting in the cut-on frequencies being moved slightly higher. The cut-on of the first vertical wave is most affected as shown in Fig. 6(a), being increased from 0 to 1 kHz by the presence of the support. It can therefore be said that the presence of the foundation does not result in large changes in the frequency–wavenumber plot at high frequencies. However, the foundation will contribute considerably to the decay rates of each wave because the damping loss factor of a rail pad is generally much higher than that of the rail itself.

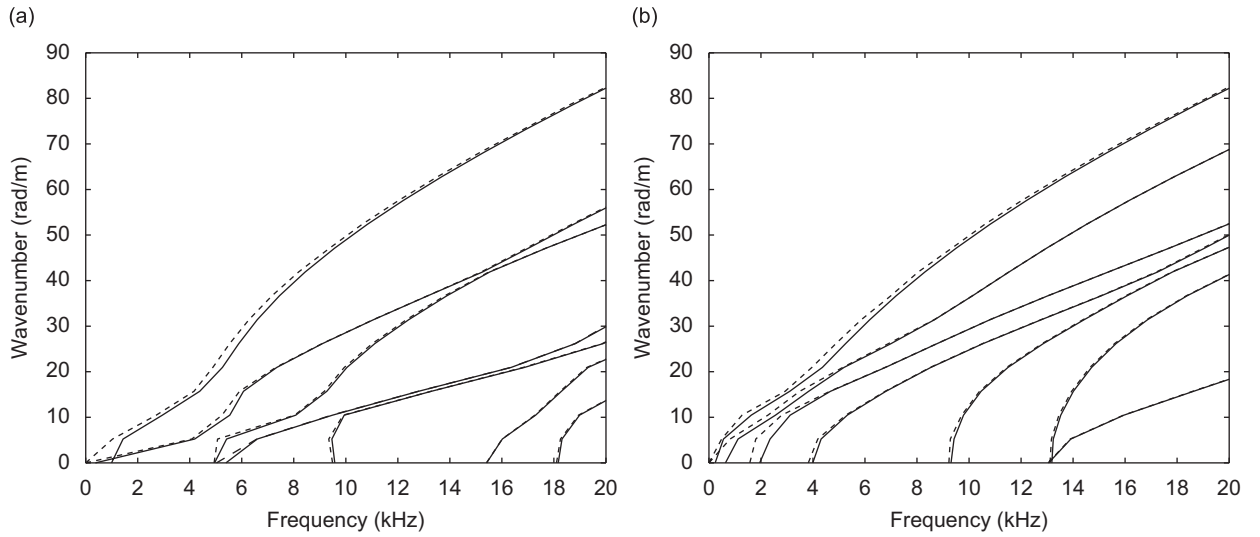

Fig. 6. Comparison of dispersion relations between free and supported rail for (a) the vertical and symmetric longitudinal waves and (b) the lateral, torsional and antisymmetric longitudinal waves. – –, free rail; ——, supported rail.

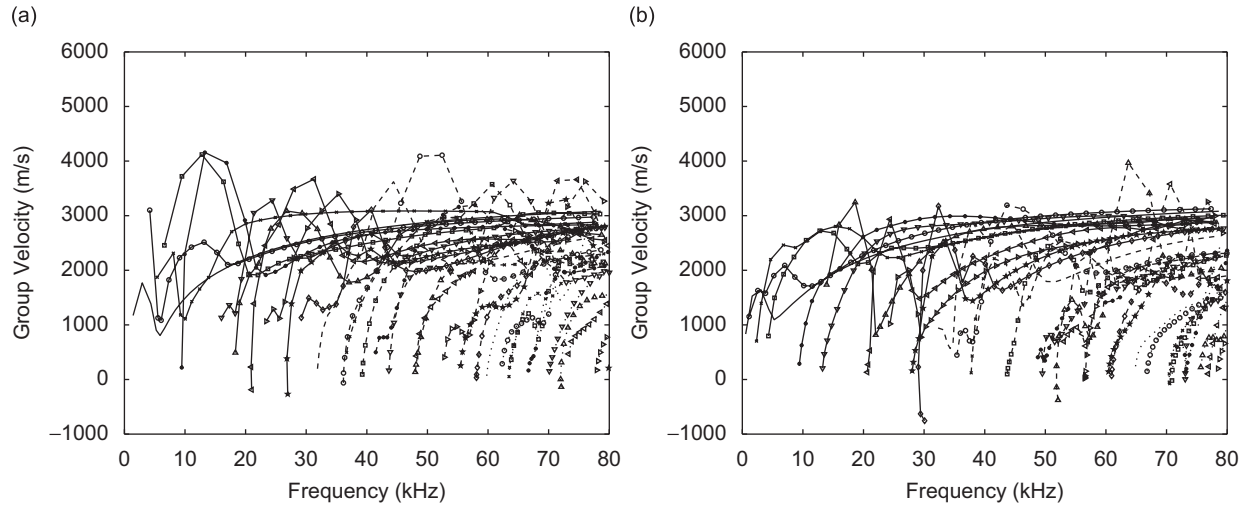

Fig. 7. Predicted group velocities obtained by FEA for (a) the vertical and longitudinal waves and (b) the lateral and torsional waves. The line styles and markers correspond to Fig. 3.

2.3. Predicted group velocities

The group velocities, c_g, of each wave can be specified from the dispersion curves by use of the relation

$$c_g = \frac{\mathrm{d}\omega}{\mathrm{d}\kappa}, \tag{2}$$

where ω is the angular frequency. In this study, the group velocity of the ith wave at the nth discrete frequency is calculated approximately by a finite difference scheme

$$(c_g^i)_n \approx \frac{\omega_{n+1}^i - \omega_{n-1}^i}{\kappa_{n+1}^i - \kappa_{n-1}^i} = \frac{\omega_{n+1}^i - \omega_{n-1}^i}{2\Delta\kappa}. \tag{3}$$

The group velocities estimated are shown in Fig. 7. The line styles and markers correspond to Fig. 3. At a cut-on frequency, the group velocity becomes zero corresponding to rigid body motion of the rail. The longitudinal waves are readily identifiable in Fig. 7 because they have group velocities approaching 5000 m/s. It seems from these group velocity figures that the velocities tend to approach a fixed value, possibly the shear wave speed, as frequency increases. The shear wave speed is about 3100 m/s for a bulk shear wave and about 2850 m/s for a shear wave in a beam with a square cross-section. In addition, negative group velocities arise around some cut-on frequencies. This negative group velocity means that for a wave travelling forwards the energy carried by the wave propagates backwards and vice versa.

Since the increment of discrete wavenumbers, Δk, is determined by the length of the rail model, a longer rail model which has an increased number of elements in the x direction will create more precise group velocity curves than those in Fig. 7 (unless Δk is so small to amplify numerical errors resulting from numerical differentiation). The cost, however, is that storage space and computing time increase dramatically due to the increased number of degrees of freedom in the FE model and this may make the analysis impractical. Accordingly, it is necessary for the FE analysis to reach a compromise between the precision of the results and the necessary computing requirements.

3. Wavenumber finite element analysis of a railway track

The FE method was used above to generate dispersion and group velocity curves even at high frequencies. This has several drawbacks for practical application, primarily the FE method requires very large models for high-frequency analysis and so imposes a large computational burden. Furthermore, considerable manual post-processing is required to build dispersion and group velocity curves from the results of the FE analysis. To overcome these difficulties, an improved numerical method called the wavenumber finite element (WFE) method is employed. Also one of its great advantages is that different wave types are readily identified and can be analysed, enabling a physical interpretation of the wave propagation in the structure under investigation.

3.1. Equation of motion

Suppose that there is an elastic structure which is infinitely long in one direction, call it the x direction, and its cross-section normal to the x-axis is uniform along x. In this model, it is possible to define a wave solution for the x direction instead of making a finite element mesh along this direction. Then time harmonic displacements, (u, v, w), of the element in three directions of (x, y, z) can be expressed with separable variables as

$$\begin{aligned} u(x, y, z, t) &= \chi(y, z) \cdot \tilde{u} e^{-j\kappa x} e^{j\omega t}, \\ v(x, y, z, t) &= \psi(y, z) \cdot \tilde{v} e^{-j\kappa x} e^{j\omega t}, \\ w(x, y, z, t) &= \xi(y, z) \cdot \tilde{w} e^{-j\kappa x} e^{j\omega t}, \end{aligned} \tag{4}$$

where t denotes time, y and z denote coordinates of the cross-section, χ, ψ and ξ define the displacements of the cross-section and $\tilde{u}$, $\tilde{v}$ and $\tilde{w}$ are scaling constants.

By using these wave solutions for the x direction in the finite element formulation, a two-dimensional finite element equation is made over a cross-sectional model, instead of a three-dimensional full structure model. The differential equation for a cross-sectional model is given by

$$\left\{ \mathbf{K}_2 \frac{\partial^2}{\partial x^2} + \mathbf{K}_1 \frac{\partial}{\partial x} + \mathbf{K}_0 - \mathbf{M} \frac{\partial^2}{\partial t^2} \right\} \mathbf{W}(x, t) = 0, \tag{5}$$

where $\mathbf{K}_2$, $\mathbf{K}_1$ and $\mathbf{K}_0$ are stiffness matrices, $\mathbf{M}$ is the mass matrix of the cross-section and $\mathbf{W}(x, t)$ is the displacement vector [12,13]. All the matrices are independent of x and are real if there is no damping.

Since $\mathbf{W}(x, t) = \tilde{\mathbf{W}} e^{j(\omega t - \kappa x)}$ as described in Eq. (4), the differential equation in Eq. (5) can be simplified to an eigenvalue problem,

$$\{\mathbf{K}_2(-j\kappa)^2 + \mathbf{K}_1(-j\kappa) + \mathbf{K}_0 - \omega^2 \mathbf{M}\} \tilde{\mathbf{W}} = 0, \tag{6}$$

where $\tilde{\mathbf{W}}$ contains the displacements of the cross-section which define the deformation shapes of waves. Here κ and ω are the only unknown variables to be identified.

This twin-parameter eigenvalue problem in κ and ω has to be solved to obtain dispersion relations. It is preferred to solve ω for a given κ since it takes less computational effort than to solve κ for a given ω [13]. Eq. (6) can be solved as a generalized eigenvalue problem for a frequency ω if a wavenumber, κ, is given. In conventional FE analysis, the increment of discrete wavenumbers, $\Delta\kappa$, is determined by the length of the model according to the relation $\pi/2L$, where L denotes the model length. In this method, however, the discrete wavenumbers can be selected arbitrarily, allowing a finer resolution.

3.2. Predicted dispersion curves

In this method, a slightly finer mesh than that used in the FE analysis is adopted to model the cross-section of the UIC60 rail. This mesh is illustrated in Fig. 8. As in the previous FE analysis, the rail pad is modelled using a continuous foundation. WFE analysis creates dispersion curves very quickly and easily, removing a large portion of the manual post-processing associated with the FE analysis. The increase in efficiency of this method implies that one could increase the complexity of the model used to represent the foundation, for example, more layers could be used. This would avoid one having to calculate the dynamic stiffness separately, because the internal resonance effects could be reproduced by the model itself. However, it was found from the simulation that this model introduces many additional waves which propagate slowly through the foundation only. In other words, if the density of the foundation is introduced, waves propagating through the rail foundation take place in the numerical solutions. Therefore, it becomes very difficult to identify the waves of interest propagating along the rail, not along the foundation. Consequently, the same foundation model is employed as before, which has zero density and constant dynamic stiffness, as a suitable foundation model in this WFE analysis. Note that the waves propagating along the foundation layer occur when the rail pad is modelled as a continuous foundation with mass. So, these internal waves would not appear if the rail pad is modelled as a discrete rail foundation.

As specified in the previous FE analysis, symmetric and antisymmetric boundary conditions were applied on the vertical centreline of the cross-section. For the track model in Fig. 8, the predicted dispersion curves are shown in Fig. 9, comparing them with the previous FE analysis results. The wavenumber increment, $\Delta\kappa$, was given as $\pi/(2 \times 0.3 \times 4)$ which is a quarter of that specified in the previous FE analysis. As a result the curves obtained from the WFE analysis are smoother. Comparison in Fig. 9 reveals a high level of agreement between the two sets of results predicted by the WFE and FE analyses.

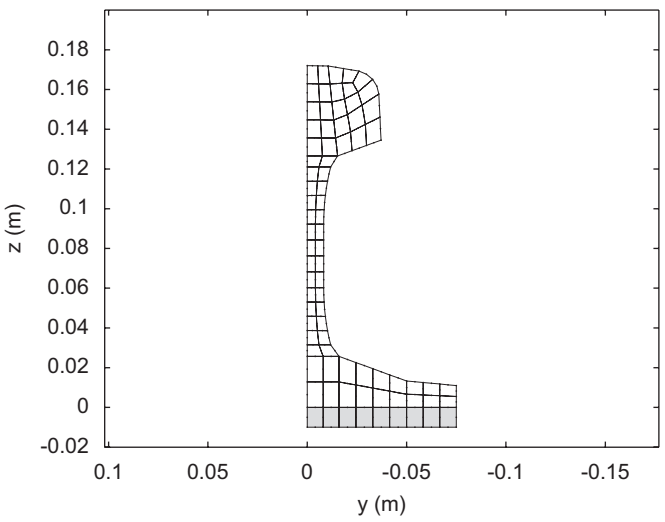

Fig. 8. The cross-sectional FE model of a rail on foundation for WFE analysis. The shaded elements represent the rail pad.

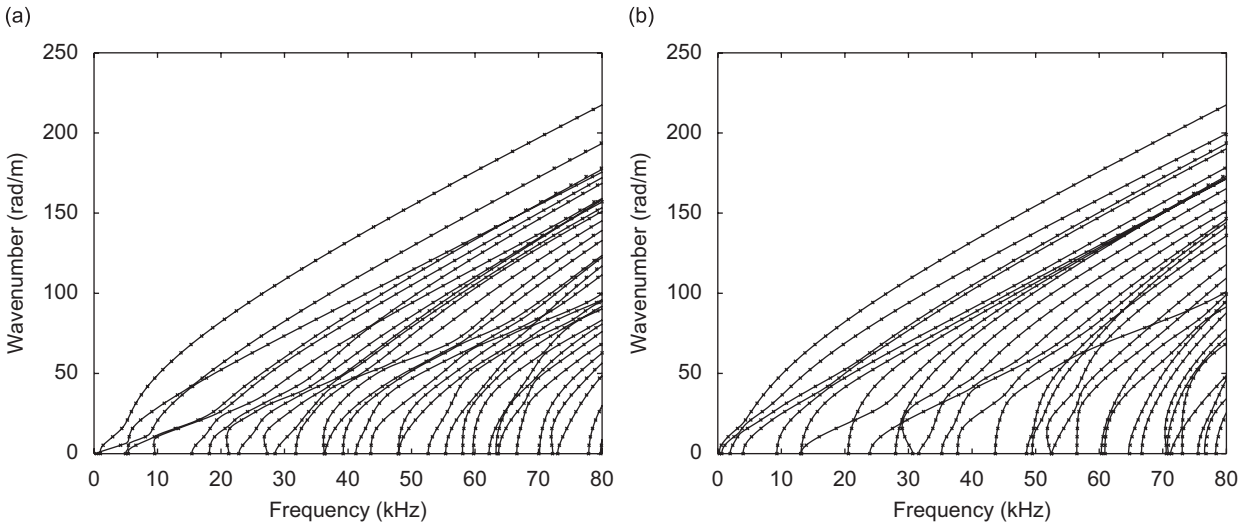

Fig. 9. Predicted dispersion curves for supported rail (a) for the vertical and symmetric longitudinal waves and (b) for the lateral, torsional and antisymmetric longitudinal waves. ——, WFE analysis; ×, FE analysis.

3.3. Predicted group velocities

In this WFE method, group velocities can also be derived theoretically from the equation of motion, Eq. (6) [13]. Since the equation has to be satisfied for any solutions of κ in the dispersion relation, then the derivative of Eq. (6) with respect to the wavenumber should always be zero. That is,

$$\frac{\partial}{\partial \kappa}\{[\mathbf{K}-\omega^2\mathbf{M}]\tilde{\mathbf{W}}\}=0, \tag{7}$$

where $\mathbf{K}=\mathbf{K}_2(-\mathrm{j}\kappa)^2+\mathbf{K}_1(-\mathrm{j}\kappa)+\mathbf{K}_0$. This derivative can be written as

$$\left[\frac{\partial}{\partial \kappa}\mathbf{K}-2\omega\frac{\partial \omega}{\partial \kappa}\mathbf{M}\right]\tilde{\mathbf{W}}+[\mathbf{K}-\omega^2\mathbf{M}]\frac{\partial}{\partial \kappa}\tilde{\mathbf{W}}=0. \tag{8}$$

By multiplying the above equation by the left eigenvector, $\tilde{\mathbf{W}}^L$, and then using the definition, $\tilde{\mathbf{W}}^{L^{\mathrm{T}}}[\mathbf{K}-\omega^2\mathbf{M}]=0$, Eq. (8) is simplified to

$$\tilde{\mathbf{W}}^{L^{\mathrm{T}}}\left[\frac{\partial}{\partial \kappa}\mathbf{K}-2\omega\frac{\partial \omega}{\partial \kappa}\mathbf{M}\right]\tilde{\mathbf{W}}=0. \tag{9}$$

Since $\mathbf{K}$ is Hermitian and $\mathbf{M}$ is real and symmetric, the left eigenvector is equal to the complex conjugate of the right eigenvector, $\tilde{\mathbf{W}}^L=\tilde{\mathbf{W}}^*$. Hence, the group velocity, c_g, can be expressed as

$$c_g=\frac{\partial \omega}{\partial \kappa}=\frac{\tilde{\mathbf{W}}^{\mathrm{H}}\mathbf{K}'\tilde{\mathbf{W}}}{2\omega\tilde{\mathbf{W}}^{\mathrm{H}}\mathbf{M}\tilde{\mathbf{W}}}, \tag{10}$$

where $^{\mathrm{H}}$ denotes Hermitian transpose and

$$\mathbf{K}'=\frac{\partial \mathbf{K}}{\partial \kappa}=-2\kappa\mathbf{K}_2-\mathrm{j}\mathbf{K}_1. \tag{11}$$

From this relation the group velocity can be easily evaluated for each wave in the dispersion diagrams.

The group velocities obtained by the WFE method are presented in Fig. 10. The different line styles and markers correspond to Fig. 3. Compared with the previous FE analysis results in Fig. 7, the FE and WFE methods yield similar results in general but the WFE method produces more accurate and smoother curves than the FE method. Now it becomes much easier to recognize each line's behaviour, particularly for the longitudinal waves which have the highest group velocities. This improved graphical result is a consequence of the finer wavenumber resolution.

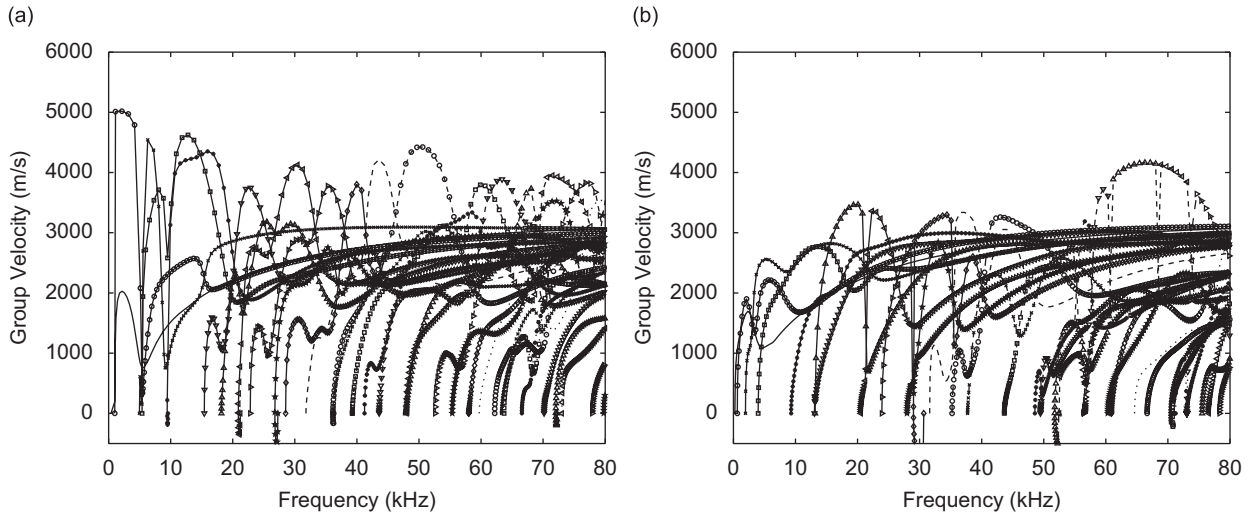

Fig. 10. Predicted group velocities for supported rail obtained by WFE analysis for (a) the vertical and symmetric longitudinal waves and (b) the lateral, torsional and antisymmetric longitudinal waves. The different line styles and markers correspond to Fig. 3.

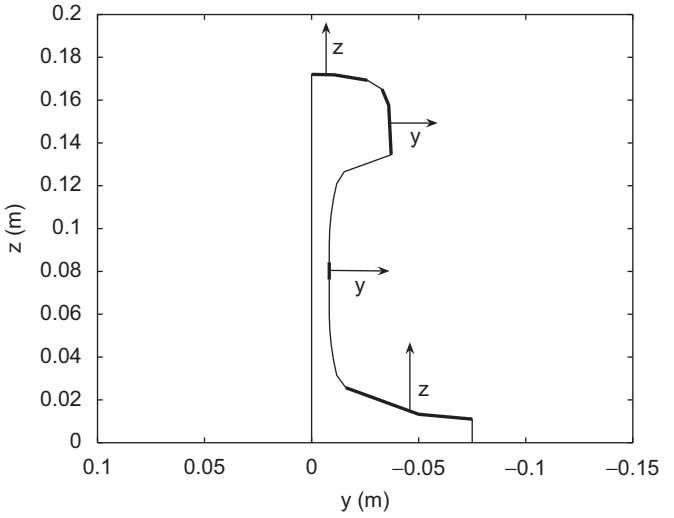

Fig. 11. Four regions and directions specified for the prediction of energy distribution on the rail surface.

4. Prediction of measurable waves on rail surface

As described previously, there are 63 different waves propagating below 80 kHz in this track model. So it will be worthwhile identifying which waves among them belong to which regions of the rail cross-section and also which ones are measurable on the rail surface. Since dynamic responses are usually measured normal to the rail surface, the energy distributions around the rail surface can provide useful information on which waves are detectable in a specific region. To achieve this, the "energy" associated with different parts of the rail surface was calculated from the predicted displacement of the track model produced by the WFE (or FE) method. For this purpose, four separate regions were specified on the rail surface as shown in Fig. 11. These are the top of the rail head, the side of the rail head, the middle of the web and the top of the foot. In this figure, y and z denote lateral and vertical directions, respectively. Then the normalized energies for each region

and each direction were predicted using

$$Q_{j,z} = \frac{(1/n_j)\sum_{n_j}|\tilde{\mathbf{W}}_{z,j}|^2}{(1/N)\sum_N\|\tilde{\mathbf{W}}_s\|^2}, \tag{12}$$

where $\tilde{\mathbf{W}}_s$ denotes displacements in all directions at nodes on the rail surface, $\|\|$ is the vector norm, $\tilde{\mathbf{W}}_{z,j}$ is displacement in the vertical z direction (and similarly for the x (longitudinal) and y (lateral) directions) at nodes belonging to the region j, n_j is the number of nodes in the region j and N is the number of nodes on the rail surface. Therefore, this quantity would depict implicitly which waves are measurable in region j among all the waves in the system. In this calculation, no information on the input force or modal participation factor is included so that all the modes are treated equally. These measurable waves predicted by Eq. (12) will be used in comparison to the measured results in subsequent sections.

The predicted dispersion curves at each region are illustrated in Fig. 12 in terms of the energy ratio given in Eq. (12). In this plotting, a threshold was established to exclude waves, which have small energy ratio, in order to make the figures more comprehensible. Only the waves which satisfy the criterion, $Q_j/\max(Q_j) > 0.1$ in each

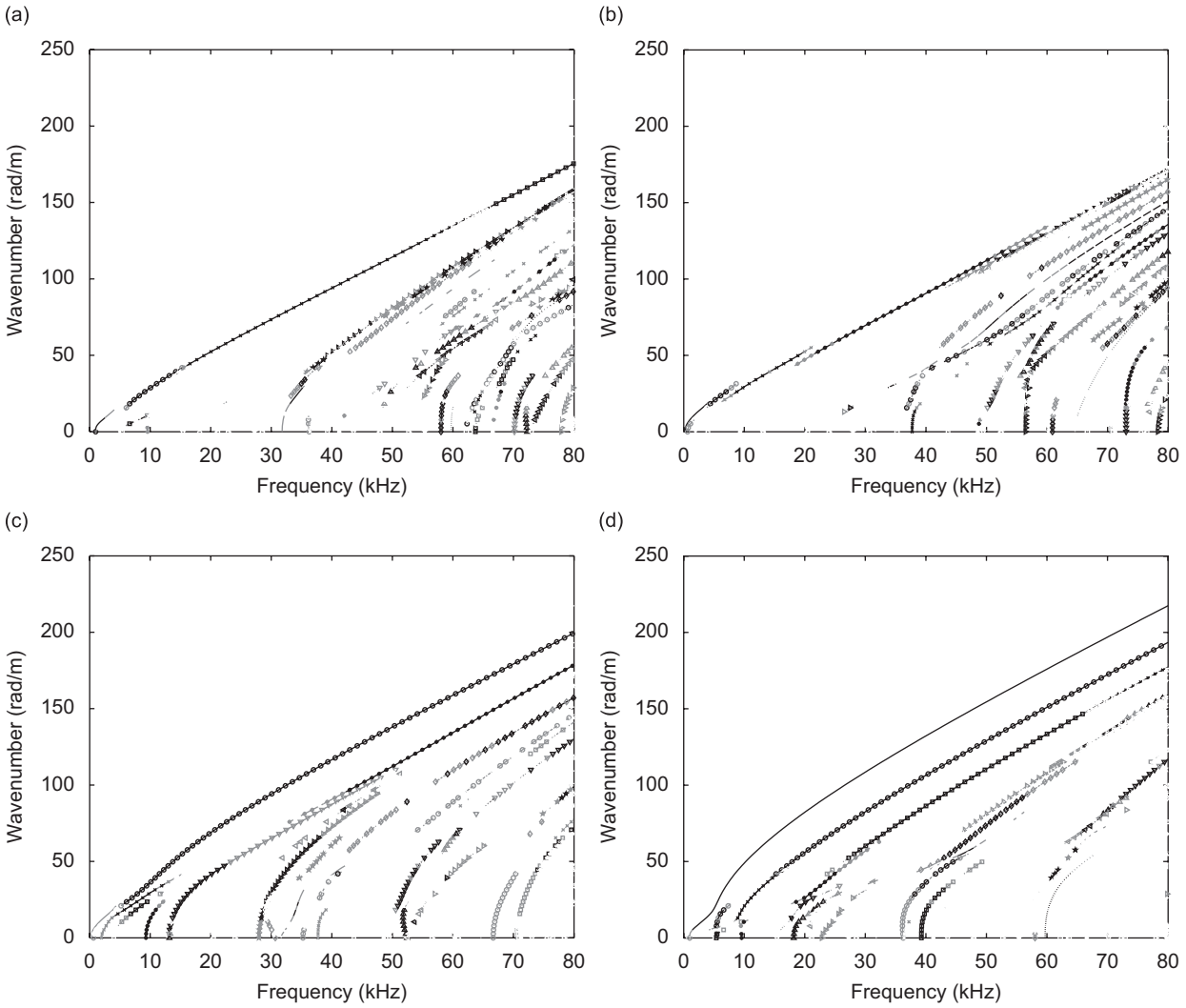

Fig. 12. Predicted dispersion curves with line intensity shown in terms of the energy for the vertical and lateral directions (a) at the top of the rail head, (b) at the side of the rail head, (c) at the middle of the web and (d) at the top of the foot. The different line styles and markers correspond to Fig. 3.

figure, are included in Fig. 12. Also in order to distinguish between the less and more measurable waves, two degrees of darkness were used to plot the curves in Fig. 12. They are grey and black, corresponding to the less and more measurable waves, respectively. The respective criteria for them were chosen as $0.1 < Q_j/\max(Q_j) \leqslant 0.2$ for the less measurable waves and $0.2 < Q_j/\max(Q_j)$ for the more measurable waves.

Fig. 12(a) reveals that only a single type of wave, i.e., the head bending wave, is dominantly measurable at the top of the rail head below 32 kHz. This is the wave shown in Fig. 4(c). Other vertical waves that are significant tend to cut-on at around 32 kHz. A similar phenomenon is obtained at the side of the rail head for the lateral direction (Fig. 12(b)) where the wave seen in Fig. 5(e) is most important. Conversely, at the middle of the web a large number of waves are present throughout the whole frequency range, but the first-order web bending wave (Fig. 5(b)) is prominent above 10 kHz. On the top of the foot, foot bending waves will possess most deformation energy. In the same manner, the group velocities at each region can be presented in terms of the energy ratio. These measurable group velocities predicted at each region will be shown later together with the measured ones.

5. Group velocity measurement on a test track

Two experiments were implemented at a short test track to validate the simulated results for the frequency region up to 80 kHz, by using an impact hammer and PZT as the exciter and accelerometers as the receivers. The test track is equipped with UIC60 rail of about 32 m in length. The rail is mounted with Pandrol Fastclips, 10 mm studded rubber rail pads and concrete sleepers surrounded by ballast.

5.1. Measurement using an impact hammer

A miniature impact hammer, PCB 086D80, was used to generate a broadband signal at one end of the rail. According to the manufacturer's specification, the excitation frequency range of this impact hammer is limited to 20 kHz. Lanza di Scalea et al. [18], however, reported that they were able to excite frequencies up to between 40 and 50 kHz with this type of hammer. Accelerometers, PCB 352C22, were used to detect propagating waves along the rail. The specification sheet indicates that this accelerometer also has a limited measurement range of up to 20 kHz. Nevertheless, the mounting resonance frequency of the accelerometer is specified as around 90 kHz. Therefore it can be used beyond 20 kHz for measuring dispersion characteristics of propagating waves as long as the measurements do not need to be calibrated.

Accelerometers were set up along the rail at various positions. Results are shown here for two positions, spaced at a distance of ten sleeper spans. They were both placed at the mid-span between two sleepers. Also, to avoid the near-field effects that take place around both ends of the rail and to diminish the contributions of the quickly decaying waves, the sensors were located in the central portion of the rail. The frequency range was limited up to 42 kHz by the data acquisition unit. In this experiment, the excitation points were less than about 10 mm away from the adjacent end of the rail. Since the frequency range was limited up to 42 kHz, the shortest wavelengths in the rail are about 63 mm at the rail head, 52 mm at the web and 46 mm at the rail foot, respectively. The phase cancellation due to the waves reflected from the adjacent end of the rail may be considerable at the rail foot at around 42 kHz because $46\,\text{mm}/4 \approx 10\,\text{mm}$. However, at other positions and at other frequencies, the phase cancellation will be negligible in this measurement. The measurement set-up is shown in Fig. 13. It should be noted that there are two welds in the rail of this test track as marked in Fig. 13. These welds may lead to wave reflections, particularly at the web and foot of the rail because there is considerable thickness change.

The excitation was applied and the responses along the rail were measured at four different positions on the cross-section, specifically, at the top and side of the rail head, middle of the web and top of the foot. In the calculation of the energy ratio in Eq. (12), it was assumed that all the modes take place equally. In practice, however, the rail response will depend on the position of the excitation which determines the excited modes. In order to make similar condition to that used in Eq. (12) in the measurement, the rail responses were acquired at the same positions on the rail cross-section as the excitation is applied. If the excitation and receiving positions are different, the rail response would appear as a combination of the energy metric in Eq. (12) for the excitation and receiving positions on the cross-section.

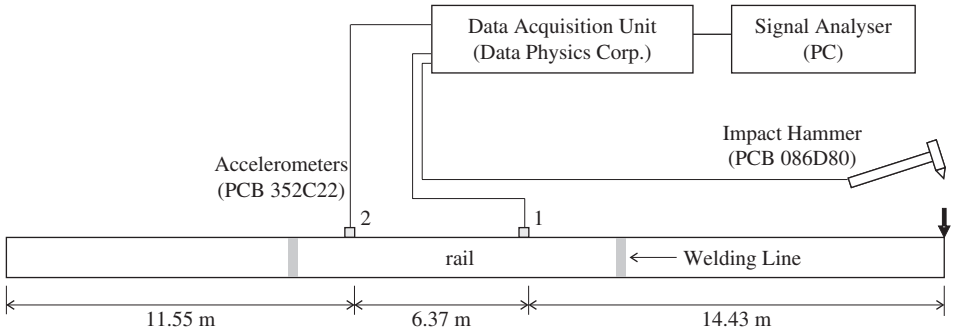

Fig. 13. Experimental set-up using a impact hammer as an exciter.

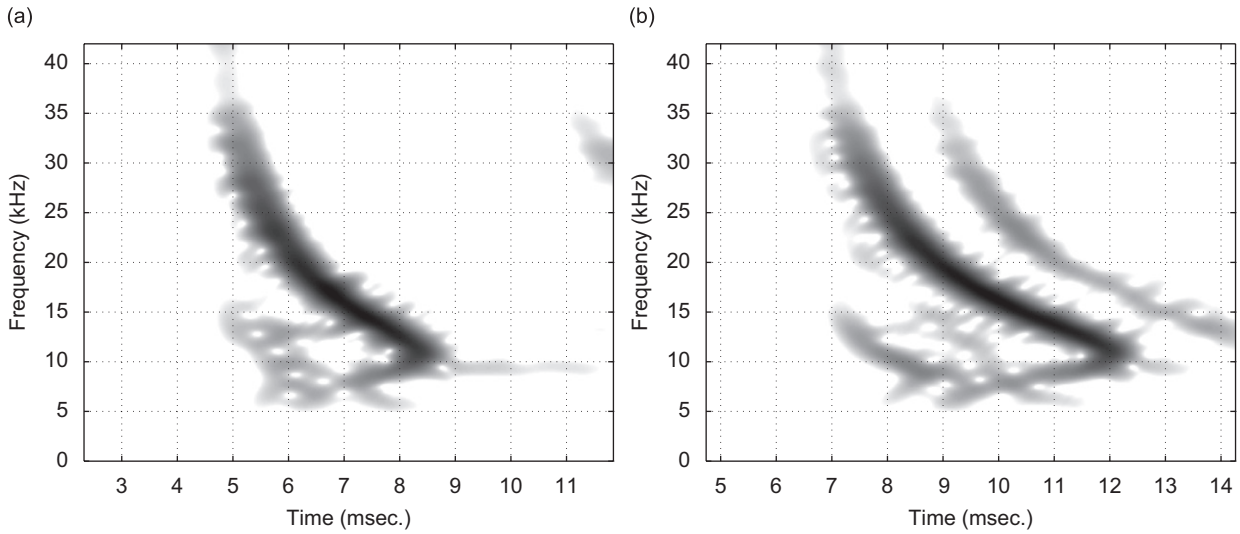

Fig. 14. Spectrograms measured at the middle of the web by (a) sensor 1 and (b) sensor 2.

The spectrogram, using the Short Time Fourier Transform [19], was used for time–frequency analysis of the measured signals. As an example, two spectrograms measured at the middle of the web are shown in Fig. 14. The range of amplitudes between black and white in this figure is 30 dB. These spectrograms present well the dispersive characteristics of the propagating waves, showing that the waves in the range 8–30 kHz carry large energy. Also it is observed from Fig. 14(b) that the welding line causes energy reflection at the web of the rail. That is to say, the wave reflected from the welding line located next to sensor 2 appears with a time delay of about 2 ms in the spectrogram. However, this sort of energy reflection due to the welding lines was not evident in data collected from the top and side of the rail head.

Since the distances between the excitation point and the receiving positions are known, the time axis of the spectrograms can be easily converted to a velocity axis using $velocity = distance/time$. Hence the time–frequency diagrams can be replotted to show frequency versus velocity. In this diagram, the velocity represents the group velocity because the energy carried by waves travels with the group velocity. The group velocity–frequency diagrams at position 1 are illustrated in Fig. 15 and compared with the simulated ones for measurable waves predicted by Eq. (12).

From this comparison, it is clear that the simulated group velocity curves correspond very well to the measured ones. Therefore, the deformation shapes of primary waves measured can be inferred from the simulated results. The wave dominantly measured at the top of the rail head was identified as a vertical bending wave propagating along the rail head as illustrated in Fig. 4(c). It has to be noted that the dip of

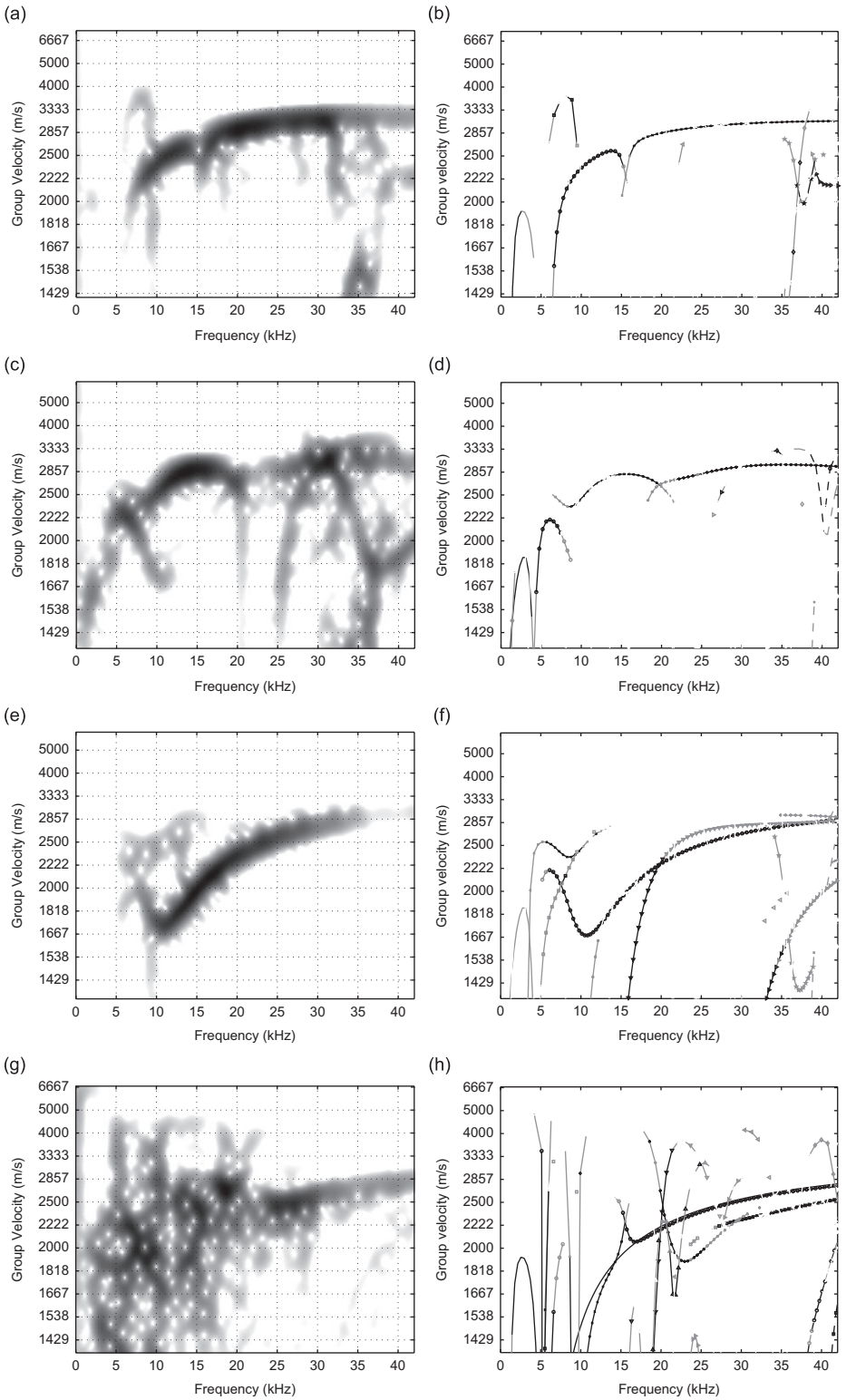

Fig. 15. Measured and predicted group velocities. (a), (b) At the top of the rail head in the vertical direction, (c), (d) at the side of the rail head in the lateral direction, (e), (f) at the middle of the web in the lateral direction and (g), (h) at the top of the foot in the vertical direction. Predictions are shown with line intensity given in terms of energy.

group velocity at 15 kHz in Fig. 15(a) and (b) results from the wave mode conversion which occurs between the second and third waves in Fig. 3(a). Meanwhile at the side of the rail head, the waves mainly measured around 2857 m/s in Fig. 15(c) tend to have global deformation as shown in Fig. 5(e). The wave measured at the middle of the web is the first-order web bending wave and its deformation shape is shown in Fig. 5(b). At the top of the foot, however, it is hard to define any characteristics of propagating waves, especially below 20 kHz because of noise contamination. This noise appears because the waves travelling along the rail foot decay very rapidly due to the energy dissipation by the rail pads. Accepting this, it shows that the measured group velocity curves correspond well to the predicted ones above 20 kHz, and the dominant wave type is the first-order foot bending wave as shown in Fig. 4(a).

5.2. Measurement using piezoceramic transducers

In this second experiment, piezoceramic transducers (PZT) were used for excitation instead of an impact hammer because the PZT can create a sharp impulse which is capable of exciting the structure up to 80 kHz. The type of PZT used in this experiment was Pz27 plate, manufactured by Ferroperm Piezoceramics A/S [20]. The dimensions of this PZT are a height of 1 mm and a square area of 12.7 mm × 12.7 mm. When a voltage is applied it expands or contracts primarily in the length and width directions, depending on the strength of the electrical field. This causes a moment to be applied at the edges due to the constraint applied by the structure, which in this case is the rail.

In terms of the structural response, the effectiveness of the excitation by PZT will be associated with how well the transducer's deformation is coupled to the structural behaviour. For example, suppose that a PZT is attached on a thick plate. If an excited wave in the plate has much longer wavelength than the attached transducer's length, then this transducer would be inefficient in generating this wave. So the transducer used here will be inefficient at creating low wavenumber (long wavelength) waves because of its small size. On the other hand, the shortest wavelengths calculated at 80 kHz in the rail are about 35 mm at the rail head, 31 mm at the web and 29 mm at the rail foot, respectively, which are two or three times longer than the length of the PZT used in the experiment. So it will not exhibit nulls at frequencies below 80 kHz.

The excitations and measurements were implemented at three locations on the rail cross-section, i.e., at the top and side of the rail head and at the middle of the web. (Measurements on the foot were excluded in this experiment because it was found from the previous experiment that waves do not travel long distances along the rail foot.) The same accelerometers as used before were utilized again in this high-frequency measurement. The measurement process was the same as carried out in the previous impact hammer test. The measurement set-up is shown in Fig. 16. In this measurement, the PZTs were attached about 5 mm away from the adjacent end of the rail. Since the shortest wavelengths in the rail below 80 kHz are around 30 mm as stated above, the

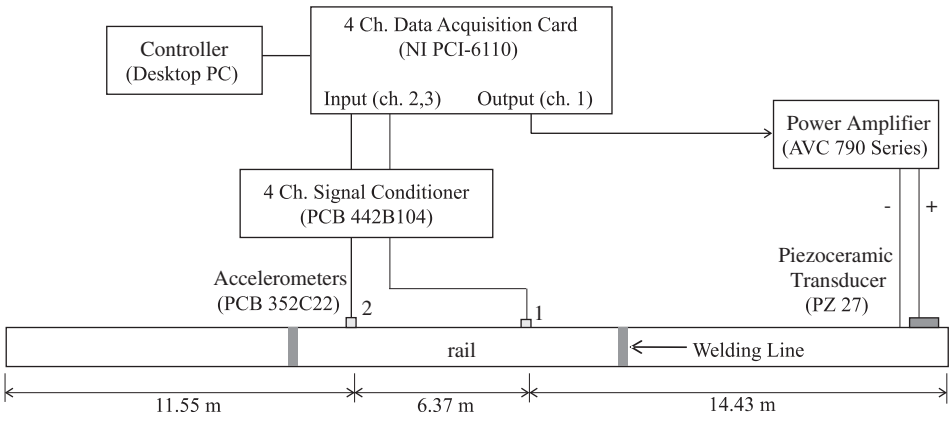

Fig. 16. Experimental set-up using piezoceramic transducers as an exciter.

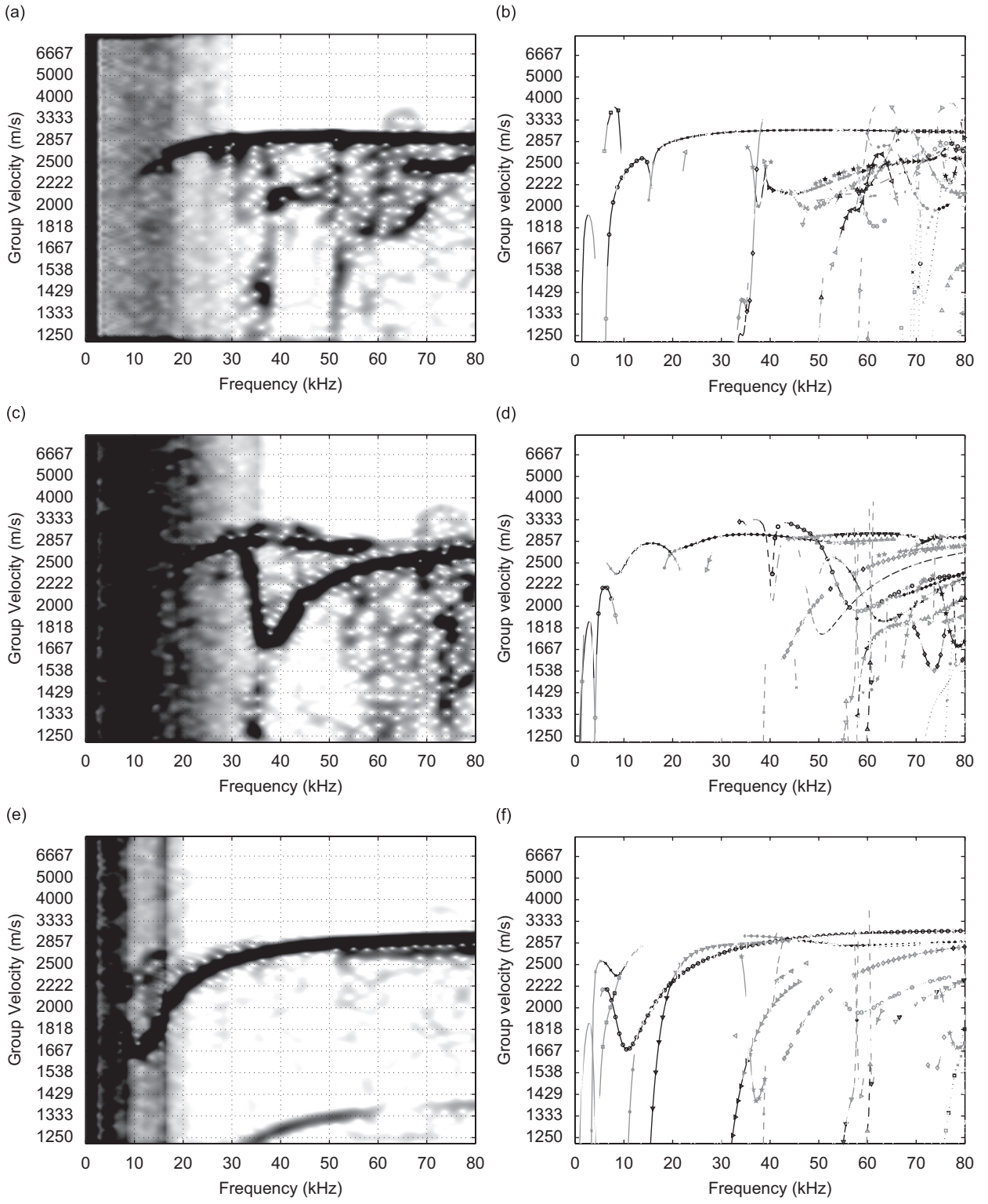

Fig. 17. Measured and predicted group velocities up to 80 kHz. (a), (b) At the top of the rail head in the vertical direction, (c), (d) at the side of the rail head and (e), (f) at the middle of the web. Predictions are shown with line intensity given in terms of energy.

phase cancellation due to the waves reflected from the adjacent end of the rail will not be significant in frequencies below 80 kHz.

Group velocity–frequency diagrams measured at position 1 are shown in Fig. 17 together with plots of the predicted values up to 80 kHz. In order to improve the graphical visibility, the measured diagrams shown in this figure were normalized by dividing each frequency column by its maximum value. As before a range of 30 dB is covered by the grey scale. It is clearly observable from Fig. 17(a), (c) and (e) that the exciter generates waves down to 20 kHz although they have a much reduced amplitude. Also it can be seen that the low-frequency region, below 20 kHz, is severely contaminated by noise. From the comparison of Fig. 17(a) with the simulated one in Fig. 17(b), it is clear that the measured group velocity curves correspond well to the simulated ones at the top of the rail head. It is clear from this measurement that the most measurable wave at the top of the rail head is still the vertical bending wave even at high frequencies. The normalized diagram shown in Fig. 17(c) clearly displays which waves are more effectively generated by the exciter than others at the side of the rail head. This effectiveness is thought to be related to the deformation shapes of the waves in the rail. Furthermore, not all possible waves will be excited by the PZT on the side of the rail head. However, it was not easy to identify the exact type of the wave measured primarily at high frequencies. Nevertheless, it could be said from Fig. 17(c) and (d) that the measured group velocity diagram agrees well with the predicted one. The group velocity diagram measured at the middle of the web exhibits fairly simple and clear curves, showing that only a single wave is primarily measurable through almost the entire frequency range with a secondary one visible just above 50 kHz. It was found by comparing Fig. 17(e) and (f) and inspecting the FE mode shapes that these two waves are the first- and third-order web bending waves. Also, the wave reflected from the welding line located right after position 2 appears in the bottom of the measured diagram.

6. Conclusions

In this work, wave propagation along the railway track was examined in the frequency region up to 80 kHz by means of FE/WFE analyses and experiments carried out on a short test track. By using the simulated mode shapes of the rail cross-section, measurable waves on the rail surface were efficiently predicted. The simulations were validated experimentally on the basis of measured group velocities. Excellent agreement between predicted and measured velocities was obtained. Also it was confirmed from this study that the WFE method is a more effective tool than the FE method for investigating a wave propagation in railway tracks. Consequently, the simulated and experimental results enabled the question: *Which wave types propagate along the rail in which part of the rail cross-section*? to be answered. The specific answers for the railway track used in this study are as follows:

- A localized head bending wave travels primarily through the rail head in the vertical direction above 15 kHz.
- At the side of the rail head, the primary wave measured is a lateral bending wave which has global deformation including the web and rail head in the lateral direction.
- The first-order web bending wave propagates dominantly through the web above 10 kHz.
- The waves propagating along the foot do not travel long distance because of the rail foundation which has a large damping effect.

It has to be noted that these results may depend on the track structures and their material properties, although rail geometry does not vary greatly in many situations.

It was observed from the measurement that a slight reflection occurs from the welds when a wave travels through the web of the rail. In practice, every track has welds along the rail though so that they will thus affect the propagation of a wave by reflecting a certain amount of travelling energy.

Acknowledgements

This work was supported by Balfour Beatty Rail Technologies.

References

[1] D.J. Thompson, Wheel-rail noise generation. part III: Rail vibration, *Journal of Sound and Vibration* 161 (1993) 421–446.
[2] D.J. Thompson, N. Vincent, Track dynamic behaviour at high frequencies, part 1: Theoretical models and laboratory measurements, *Vehicle System Dynamics Supplement* 24 (1995) 86–99.
[3] N. Vincent, D.J. Thompson, Track dynamic behaviour at high frequencies, part 2: Experimental results and comparisons with theory, *Vehicle System Dynamics Supplement* 24 (1995) 100–114.
[4] L. Gavric, Computation of propagative waves in free rail using a finite element technique, *Journal of Sound and Vibration* 183 (1995) 531–543.
[5] L. Gry, Dynamic modelling of railway track based on wave propagation, *Journal of Sound and Vibration* 195 (1996) 477–505.
[6] J.L. Rose, M.J. Avioli, W.-J. Song, Application and potential of guided wave rail inspection, *Insight* 44 (2002) 353–358.
[7] J.L. Rose, M.J. Avioli, P. Mudge, R. Sanderson, Guided wave inspection potential of defects in rail, *Proceedings of Railway Engineering 2002, Fifth International Conference and Exhibition*, London, UK.
[8] D.J. Thompson, Experimental analysis of wave propagation in railway tracks, *Journal of Sound and Vibration* 203 (1997) 867–888.
[9] D.J. Ewins, *Modal Testing: Theory and Practice*, Research Studies Press Ltd., Letchworth, 1984.
[10] T. Hayashi, W.-J. Song, J.L. Rose, Guided wave dispersion curves for a bar with an arbitrary cross-section, a rod and rail example, *Ultrasonics* 41 (2003) 175–183.
[11] P. Wilcox, M. Evans, D. Alleyne, B. Pavlakovic, K. Vine, P. Cawley, M. Lowe, Long range inspection of rail using guided waves, *Proceedings of Railway Engineering 2002, fifth International Conference and Exhibition*, London, UK, 2002.
[12] C.-M. Nilsson, Waveguide Finite Elements Applied on a Car Tyre. Ph.D. Thesis, KTH, Stockholm, 2004.
[13] S. Finnveden, Evaluation of modal density and group velocity by a finite element method, *Journal of Sound and Vibration* 273 (2004) 51–75.
[14] I. Bartoli, A. Marzani, F. Lanza di Scalea, E. Viola, Modeling wave propagation in damped waveguides of arbitrary cross-section, *Journal of Sound and Vibration* 295 (2006) 685–707.
[15] K. Knothe, S.L. Grassie, Modelling of railway track and vehicle/track interaction at high frequencies, *Vehicle System Dynamics* 22 (1993) 209–262.
[16] C.M. Harris, *Shock and Vibration Handbook*, third ed., McGraw-Hill, New York, 1988 (Chapter 10).
[17] N.C. Perkins, C.D. Mote Jr., Comments on curve veering in eigenvalue problems, *Journal of Sound and Vibration* 106 (1986) 451–463.
[18] F. Lanza di Scalea, J. McNamara, Ultrasonic NDE of railroad tracks: air-coupled cross-sectional inspection and long-range inspection, *Insight* 45 (2003) 394–401.
[19] S. Qian, D. Chen, *Joint Time–Frequency Analysis: Methods and Applications*, Prentice-Hall, Englewood Cliffs, NJ, 1996.
[20] http://www.ferroperm-piezo.com/ (date accessed: 20 September 2006).